

## Topical Review

# Photon management for enhanced open-circuit voltage in nanostructured solar cells

S Sandhu<sup>1</sup>, Z Yu<sup>2</sup> and S Fan<sup>1</sup><sup>1</sup> Department of Electrical Engineering, Stanford University, Stanford, CA 94305, USA<sup>2</sup> Department of Electrical and Computer Engineering, University of Wisconsin-Madison, Madison, WI 53706, USAE-mail: [sunil.sandhu@stanford.edu](mailto:sunil.sandhu@stanford.edu) and [zyu54@wisc.edu](mailto:zyu54@wisc.edu)

Received 9 June 2014, revised 23 June 2015

Accepted for publication 7 August 2015

Published 29 September 2015

**Abstract**

We review the recent progress on using pure photonic engineering for voltage enhancement of nanostructured solar cells. These works use a detailed balance analysis for the current–voltage modeling of their devices, while taking into account of intrinsic material nonidealities to determine their fundamental limiting performances. The physics of voltage enhancement in these nanostructures is elucidated and shown to be related to the suppression of thermal emission in the immediate vicinity of the material electronic bandgap. We also review a recent work on using thermal emission suppression in a single material tandem cell configuration to overcome the Shockley–Queisser limit.

Keywords: nanostructured solar cells, photon management, Shockley–Queisser limit

(Some figures may appear in colour only in the online journal)

**1. Introduction**

Nanostructured solar cells have been shown to be promising candidates for third-generation photovoltaics with advantages that include easily scalable manufacturing, lower cost and tunable optical absorption [1–9]. In recent years, there has been increased interest in the study of these nanostructured solar cells as a way to improve solar cell efficiency [10, 11]. These works have mainly focussed on photon management, particularly the tailoring of the absorption properties of the solar cell with the specific goal of enhancing its short-circuit current performance [12–22, 23]. However, the fundamental limiting performance of any solar cell is determined by the thermodynamic constraints on both its current and voltage. It is therefore of interest to complement these studies on current enhancement with a better understanding of the solar cell's voltage behavior.

The conventional way of enhancing a solar cell's voltage performance is by improving the quality of material used or through material engineering [24–32]. On the other hand, recent works have shown that in the case of nanostructured cells, photon management can also play a significant role in enhancing the nanostructured cell's voltage performance over that of a bulk cell [6, 33–38]. Niv *et al* [38] did one such study on a GaAs thin film with nanoscale thickness and showed that the open-circuit voltage of the thin film can be significantly enhanced beyond that of a bulk cell. However, [38] only considered a flat thin film and, therefore, there was a significant penalty to the absorption and short-circuit current performance of their structure. One natural approach to enhance the absorption of the thin film structure is by incorporating light trapping into it [39]. This was realized in the work of [37], which showed that the significant voltage enhancement over a bulk cell can indeed be preserved after introducing light trapping

into the nanoscale thin film structure. In addition, [37] also elucidated the underlying physics of open-circuit voltage enhancement by showing that it is related to the *suppression* of thermal emission in the immediate frequency range of the thin film's electronic bandgap. In fact this method for voltage enhancement can also be applied to other nanostructure geometries. For example, [34] showed that a single nanowire can have a much higher open-circuit voltage as compared to that of a bulk cell, and that the voltage enhancement is related to the removal of resonances in the immediate vicinity of the wire's electronic bandgap.

Furthermore, [35] highlighted that the above works on voltage enhancement through thermal emission suppression also has applications in multi-junction cells. The authors in [35] showed that by controlling the top cell's near bandgap thermal emission in a tandem cell configuration constructed from a single material, one can actually exceed the Shockley–Queisser limit on efficiency. This was the first work that used a pure photonic approach to overcome the Shockley–Queisser limit in a single semiconductor structure.

In this article, we will review all the above works on photon management for voltage enhancement. The outline of this review is as follows. We will start in section 2 with an analysis of the thermodynamic constraint to voltage enhancement in an ideal solar cell within the radiative limit. We will show through this thermodynamic analysis that thermal emission suppression in the immediate vicinity of the cell's electronic bandgap can enhance its open-circuit voltage. In section 3, we will review the detailed balance analysis that will be used to calculate the current–voltage characteristics of nanophotonic structures. And section 4 presents the results of applying this detailed balance analysis in the design of some nanostructures for voltage enhancement. The physics of voltage enhancement in these nanostructures is then elucidated in section 5. Finally, in section 6 we will present a recent work on a single material tandem cell design that uses voltage enhancement to overcome the Shockley–Queisser limit.

## 2. The thermodynamic constraint to voltage enhancement in nanophotonic structures

We first analyze the thermodynamic limit to open-circuit voltage enhancement in an ideal solar cell that behaves like a blackbody above some *photonic bandgap* energy  $E'_g$ , and has zero absorptivity below  $E'_g$ . In the case of a semiconductor cell with electronic bandgap  $E_g$ ,  $E'_g \geq E_g$ .

In order to simplify the analysis in this section, we will only consider radiative mechanisms within our cell, i.e. at open-circuit the only carrier loss mechanism is radiative recombination. We note that this simplification is justified for the GaAs nanophotonic solar cell examples that will be considered in this review article, since the radiative processes in these nanoscale GaAs cells strongly dominates over the non-radiative processes (section 3.1).

When our solar cell is operating at open-circuit, i.e. output current is zero, the principle of detailed balance states that at equilibrium the cell's total photon absorption rate has to equal

its total photon emission rate [40]. Starting from this detailed balance equation, one can derive the following approximation for the chemical potential per emitted photon [41]:

$$qV_{oc} \approx E'_g \left(1 - \frac{T_c}{T_s}\right) + kT_c \log\left(\frac{T_s}{T_c}\right) - kT_c \log\left(\frac{f_c}{f_s}\right) \quad (1)$$

where  $V_{oc}$  is the open-circuit voltage of the cell,  $q$  is the electron charge,  $k$  is the Boltzman constant,  $T_c$  is the cell's temperature, and  $T_s$  is the sun's temperature.  $f_s = \int_{\Omega_s} d\Omega \cos(\theta)$  is the geometrical factor associated with the solid angle  $\Omega_s$  subtended by the incident sun radiation,  $f_c = \int_{\Omega_c} d\Omega \cos(\theta)$  is the geometrical factor associated with the solid angle  $\Omega_c$  subtended by the cell's emitted radiation, and  $\theta$  is the polar angle of the incident or emitted light's propagation vector. In deriving (1), we have made the assumption that  $\frac{E'_g}{kT_s}, \frac{E'_g}{kT_c} \gg 1$ .

Equation (1) describes the different components of our ideal solar cell's  $V_{oc}$  performance in the radiative limit: the first term in the right hand side of (1) represents the *Carnot efficiency* of conversion from temperature  $T_s$  to  $T_c$  of a monochromatic beam with photon energy  $E'_g$ , the second term represents the correction that accounts for the finite bandwidth of the absorbed beam and emitted beam spectra, and the last term represents the open-circuit voltage reduction due to the expansion of the photon beam from an incoming solid angle  $\Omega_s$  to an outgoing solid angle  $\Omega_c$  [41]. Therefore, (1) yields the  $V_{oc}$  of a solar cell maintained at temperature  $T_c$  with photonic bandgap energy  $E'_g$ , and with the angular restriction factor  $f_c/f_s$ .

We notice from (1) that for a cell operating at a fixed temperature  $T_c$ , we can enhance its open-circuit voltage by either of the following two strategies: (A) reducing the cell's emission angle and thus its angular restriction factor  $f_c/f_s$  (with the constraint  $f_c \geq f_s$  [41]), or (B) by increasing the cell's *photonic bandgap* energy  $E'_g$ . The use of strategy (A) for voltage enhancement was recently presented in [42] using a nanoscale GaAs thin film design with a top layer *coupler* that restricts the nanostructure's emission angle. The authors in [42] showed using a detailed balance analysis that such a nanostructure with limited emission angle can result in a large improvement of the cell's current–voltage performance.

On the other hand, there have been various recent studies on voltage enhancement in nanophotonic structures using strategy (B) [34–38]. The general idea in these works involve using photonic design to suppress the absorption and thus the thermal emission of the nanostructure in the immediate vicinity of its electronic bandgap. The result of this absorption suppression is an increase in the nanostructure's photonic bandgap  $E'_g$  and therefore its open-circuit voltage. In the following sections, we will review some of these works on voltage enhancement using absorption suppression.

## 3. Detailed balance analysis for determining the voltage performance of nanophotonic structures

The performance of any solar cell is characterized by its current–voltage relationship. In the case of a bulk structure,

there have generally been two complementary methods to determine this current–voltage relationship: (A) performing a combined electrical and optical modeling of the structure, including its detailed carrier dynamics, and (B) using the principle of detailed balance to determine the limiting efficiency of the structure while taking into account of only the intrinsic material non-idealities. Each of these approaches is important. Particularly, the first approach is vital to understanding the detailed performance of a particular structure, while the second approach provides the fundamental limiting performance in terms of efficiency for a given class of structures.

In order to determine the fundamental limiting performance of nanophotonic solar cells, we will need to pursue method (B), i.e. an analysis based on the principle of detailed balance. Niv *et al* [38] performed one such analysis by a direct calculation of the thermal emission of thin film cells using the fluctuation-dissipation theorem [43]. However, it is well known that such a direct calculation is quite involved for nanophotonic structures [44].

In the following, we will outline an alternative approach that was presented in [34, 37] for the detailed balance analysis of nanophotonic solar cells. In order to determine the current–voltage characteristics of the nanostructure, this approach only requires the cell’s absorption spectra at all angles of incidence, which one routinely calculates in the optical modeling of a solar cell. This approach can, moreover, be readily generalized to include intrinsic material non-idealities.

The alternative approach presented in [34, 37] is based on the following detailed balance equation that is applicable to all solar cells in general [40]:

$$F_g - F_c(V) + R(0) - R(V) - I/q = 0 \quad (2)$$

where  $V$  is the voltage across the solar cell,  $F_g$  and  $F_c(V)$  are the rates of radiative hole–electron pair generation and recombination, respectively, while  $R(0)$  and  $R(V)$  are the rates of non-radiative hole–electron pair generation and recombination, respectively.  $I$  is the current generated by the cell.

We next assume that the solar cell is operating at the ambient temperature  $T_c = 300$  K, and under direct sunlight with an incident solar photon rate  $S(E)$  per unit bandwidth per unit frequency at the photon energy  $E$ . In this scenario, the total radiative generation rate is given by:

$$F_g = F_s + F_{co} \quad (3)$$

where  $F_s$  and  $F_{co}$  are the radiative generation rates due to the incoming direct sunlight and surrounding ambient blackbody radiation, respectively.  $F_s$  is given by:

$$F_s = \int_{E_g}^{\infty} dE S(E) \sigma(E, \theta = 0, \phi = 0) \quad (4)$$

where the integration is taken over all photon energies above the cell’s material bandgap  $E_g$ . For all the calculations in this article, we use the AM 1.5 global spectrum standard [45] for  $S(E)$ .

The definition of  $\sigma(E, \theta, \phi)$  in (4) depends on the geometry of the solar cell. For example, in the cases of a planar solar cell (figures 1(a) and (b)),  $\sigma(E, \theta, \phi)$  has the form:

$$\sigma(E, \theta, \phi) = A \times a(E, \theta, \phi) \quad (5)$$

where  $A$  is the top surface area of the cell, and  $a(E, \theta, \phi)$  is the direction dependent absorption coefficient spectra of the cell.  $\theta$  and  $\phi$  are the polar angle and azimuthal angle, respectively, of the incident light’s propagation vector.

On the other hand, in the case of a nanowire geometry (figure 2(a)),  $\sigma(E, \theta, \phi)$  is the cell’s direction dependent absorption cross-section spectra [46].  $\theta$  is the angle that the incident light’s propagation vector makes with the normal to the wire’s longitudinal axis, while  $\phi$  is the azimuthal angle of the propagation vector.

In (3), the radiative generation rate due to the surrounding blackbody at ambient temperature  $T_c$  is given by [47, 48]:

$$F_{co} = \int_0^{2\pi} d\phi \int_0^{\theta_u} d\theta \int_{E_g}^{\infty} dE \quad (6)$$

$$\Theta(E, T_c) \sigma(E, \theta, \phi) \cos(\theta) \sin(\theta)$$

$$\Theta(E, T) = \frac{2E^2}{h^3 c^2} \left[ \exp\left(\frac{E}{kT}\right) - 1 \right]^{-1} \quad (7)$$

where  $\Theta(E, T_c)$  is Planck’s law [47] for the the surrounding blackbody incident spectral irradiance,  $h$  is Planck’s constant, and  $c$  is the speed of light in vacuum. The upper limit of the integration over  $\theta$  in (6) are  $\theta_u = \pi$  and  $\theta_u = \frac{\pi}{2}$  in the examples of the nanowire and thin film structures, respectively.

The radiative recombination rate of the nanophotonic cell in (2) relates to the voltage  $V$  across the cell as follows [40]:

$$F_c(V) = F_{co} \exp\left(\frac{qV}{kT_c}\right) \quad (8)$$

where we have used Kirchhoff’s law [47, 48] to relate the cell’s thermal equilibrium recombination rate to the radiative generation rate  $F_{co}$  due to a surrounding blackbody at the temperature  $T_c$  of the cell.

The cell’s short-circuit current  $I_{sc}$  can be calculated by setting  $V = 0$  in (2) [40]:

$$I_{sc} = qF_s. \quad (9)$$

And the open-circuit voltage  $V_{oc}$  can be solved from the following expression that is obtained by setting  $I = 0$  in (2):

$$qF_g + R(0) = qF_c(V_{oc}) + R(V_{oc}). \quad (10)$$

From equations (2)–(12), we see that calculating the absorption cross-section spectra  $\sigma(E, \theta, \phi)$  over all angles is sufficient for the detailed balance analysis of any nanostructured solar cell. This absorption spectra controls both the solar cell’s absorption and emission properties that enter into the Shockley–Queisser’s analysis [40]. For all the nanostructure geometries we will study in the following sections, the absorption spectra can be readily calculated using, for example, available computation tools discussed in [46, 49, 50].

### 3.1. Non-radiative losses

For the GaAs solar cells that we exclusively consider in this review article, the non-radiative processes in (2)

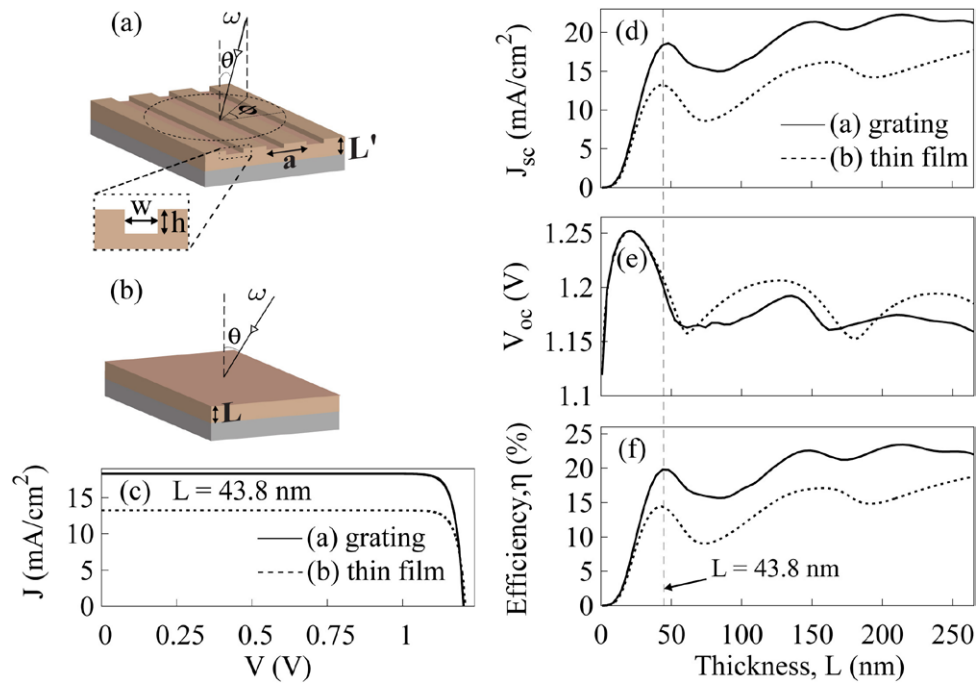


**Figure 1.** Comparison of current density-voltage ( $J$ - $V$ ) characteristics between (a) GaAs grating nanostructure and (b) GaAs thin film. The GaAs layer (gold color) is on a perfect reflecting back surface (grey color). Thickness of GaAs layer in (b) is  $L$ , while effective thickness of GaAs layer in (a) is  $L = \left(1 - \frac{wh}{L'a}\right)L'$  where  $L'$  is its actual thickness,  $a$  is its periodicity, and the air groove has width  $w$  and depth  $h$  (see inset). Arrows in (a) and (b) indicate the propagation direction of an incident plane wave with frequency  $\omega$ , and polar angle  $\theta$ . (a) also includes the azimuthal angle  $\phi$ . (c) Plots of  $J$ - $V$  characteristics for the structures in (a) and (b) with dimension  $L = 43.8$  nm. (d)–(f) Plots comparing the following characteristics versus dimension  $L$  of the structures (a) and (b): (d) short-circuit current density  $J_{sc}$ , (e) open-circuit voltage  $V_{oc}$ , and (f) efficiency  $\eta$ . In (c)–(f), the grating structure has a periodicity  $a = 456$  nm, and air-groove dimensions ( $w = 0.24 a$ ,  $h = 0.52 L'$ ). Reprinted with permission from [37]. Copyright 2012 The Optical Society.

typically includes Auger recombination, the defect mediated Shockley–Read–Hall effect, and surface recombination [51–57]. Furthermore, since our goal is to establish an understanding of how optical physics influences the solar cell's performance, following [58] we idealize to the case of a defect free GaAs cell with perfect surface passivation. Under these conditions, the only important non-radiative mechanism in our detailed-balance analysis is Auger recombination. Furthermore, we also assume that our cell is approximately intrinsic under illumination, which results in the following minimized Auger recombination rate [58–60]:

$$R(V) = (C_n + C_p) L n_i^3 \exp\left(\frac{3qV}{2kT_c}\right) \quad (11)$$

where  $C_n$  ( $C_p$ ) is the conduction-band (valence-band) Auger coefficient,  $L$  is the thickness of the solar cell, and  $n_i$  is the intrinsic carrier concentration.

Although Auger recombination is included in all of the calculations below, we note that for the GaAs solar cells considered in this article, the radiative rate dominates over the non-radiative rate. Accordingly, the  $V_{oc}$  in equation (10) can be approximated as follows:

$$V_{oc} \approx \frac{kT_c}{q} \log\left(\frac{F_g}{F_{co}}\right). \quad (12)$$

This approximation has been validated for micron thick solar cells in [61]. Moreover, using this approximation, we calculate a  $V_{oc}$  of 1.12 V for a bulk GaAs, which is in consistency with the results in [38]. However, we emphasize that one cannot, in general, neglect non-radiative recombination for most materials, and therefore one should not use (12) in general. For example, in the case of Si solar cells, the contribution from non-radiative recombination in (10) is significant when compared to radiative recombination [60].

#### 4. Application of detailed balance analysis to some GaAs nanostructures

In the following, we will present the results of applying the detailed balance analysis to calculate the current–voltage characteristics of some nanostructure geometries. The nanostructure geometries studied include the flat thin film from [37, 38], patterned thin film from [37], and a single nanowire from [34].

##### 4.1. Nanoscale flat thin film solar cell

We first present the results of applying the detailed balance approach in calculating the current density–voltage ( $J$ - $V$ ) characteristics associated with the absorption spectra of a flat GaAs thin film nanostructure shown in figure 1(b). The



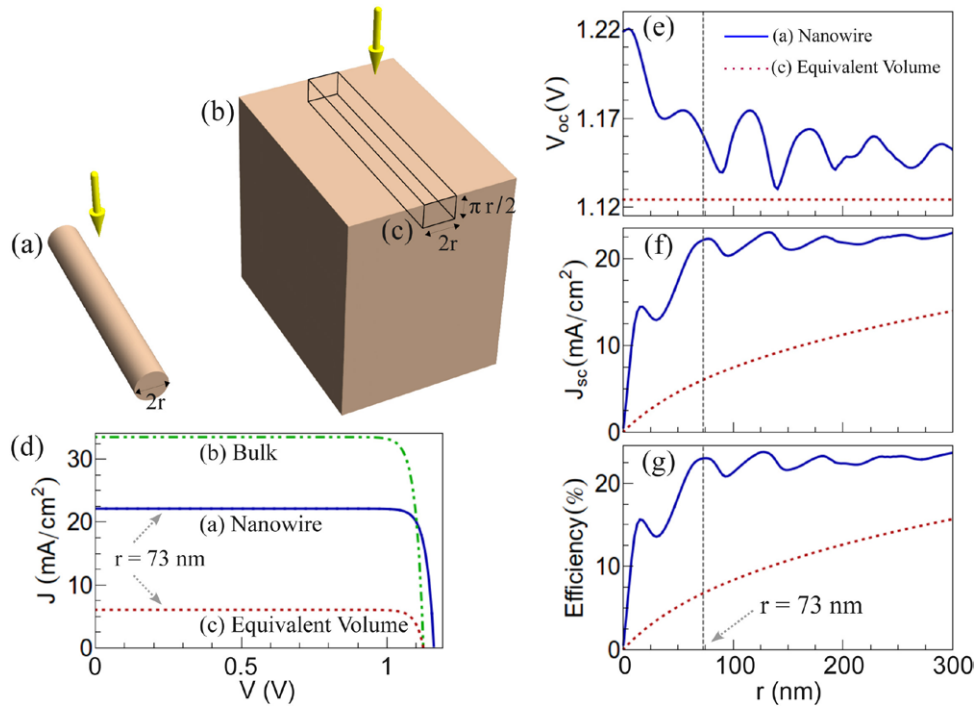


**Figure 2.** Comparison of current density-voltage ( $J$ - $V$ ) characteristics between (a) GaAs single nanowire, (b) GaAs bulk structure, and (c) an equivalent rectangular volume portion (solid black line) located at the top surface of the GaAs bulk structure. The yellow arrows indicate the direction of the incident sunlight. (d) Plots showing the  $J$ - $V$  characteristics associated with structures (a)–(c), with dimension  $r = 73$  nm for (a) and (c). (e)–(g) Plots comparing the following characteristics versus dimension  $r$  for structures (a) and (c): (e) open-circuit voltage  $V_{oc}$ , (f) short-circuit current density  $J_{sc}$ , and (g) efficiency. Reprinted with permission from [34]. Copyright 2014 American Chemical Society.

current density  $J$  here is defined as the current  $I$  in (2) per unit surface area of the thin film.

The dashed line in figure 1(c) shows the  $J$ - $V$  curve of a flat thin film with thickness  $L = 43.8$  nm. One remarkable feature of this result is that the nanoscale thin film has a  $V_{oc}$  of 1.21 V, which is significantly higher than the 1.12 V  $V_{oc}$  value for a bulk cell [38]. The result here indicates the important potential of using nanostructures for enhancing solar cell performance. However, notwithstanding this strong voltage performance, the  $J_{sc}$  of the flat thin film is significantly lower over that of the bulk cell [58]. One possible way of enhancing the  $J_{sc}$  of the thin film is to introduce light trapping to the nanostructure [39].

#### 4.2. Nanoscale patterned thin film solar cell

We next incorporate light trapping into the thin film by patterning its top surface with a one dimensional grating as shown in figure 1(a). Figure 1(c) includes the  $J$ - $V$  characteristics of an optimized grating thin film nanostructure with the same amount of absorbing material as the  $L = 43.8$  nm unpatterned thin film discussed in section 4.1. We see that the  $J_{sc}$  of the grating structure is significantly enhanced over that of the flat thin film. Furthermore, the grating structure maintains the  $V_{oc}$  enhancement of the flat thin film over that of the bulk cell.

Figures 1(d)–(f) compares the  $J_{sc}$ ,  $V_{oc}$  and efficiency  $\eta$  of the flat thin film and grating nanostructures for a wide range of thicknesses  $L$ . The efficiency here is defined as  $FF \frac{J_{sc} V_{oc}}{P_{inc}} \times 100\%$

where  $P_{inc}$  is the total incident sun radiation power per unit cell area, and FF is the cell's fill-factor [40].

We see that, over the thicknesses  $L$ , the grating structure generally has a large current enhancement over that of the flat thin film while maintaining the voltage enhancement of the flat thin film over that of the bulk cell. Consequently, there is a large efficiency enhancement in the case of the grating structures.

#### 4.3. Single nanowire solar cell

As a final example, we present the  $J$ - $V$  characteristics associated with the calculated absorption cross-section spectra for a single nanowire with radius  $r$  (figure 2(a)). The current density  $J$  for the nanowire is defined as:

$$J = I/G \quad (13)$$

where  $G = 2r \times (1 \text{ meter})$ , i.e. a unit length nanowire's cross-sectional area projected onto a plane whose normal is perpendicular to the wire's longitudinal axis [46]. Figure 2(d) compares the  $J$ - $V$  curve of an optimized GaAs nanowire with that of a GaAs bulk cell with perfect anti-reflection coating. Similar to the case of the nanoscaled thin films in sections 4.1 and 4.2, the nanoscale sized wire also has a significantly enhanced  $V_{oc}$  over that of the bulk cell. Moreover, figure 2(e) shows that this large voltage enhancement occurs over a wide range of radii.

Figure 2(d) also includes a volumetric comparison of the nanowire's generated current density with the current density associated with the contribution to the overall performance of

the bulk cell from a hypothetical equivalent volume portion located at the bulk cell's top surface. In this equivalent volume comparison, we assume that incident sunlight on the bulk cell undergoes single-pass absorption given by the following absorption coefficient in (5):

$$a(E, \theta = 0, \phi = 0) = 1 - \exp\left[-4\pi \frac{E}{hc} |\kappa(E)| L\right] \quad (14)$$

where  $\kappa(E)$  is the material extinction coefficient at the photon energy  $E$  [62]. We note that the equivalent volume construct here is not used in the voltage comparison with the nanowire. For such a voltage comparison, we directly compare the nanowire's voltage with that of the bulk cell.

Figure 2(d) shows that the nanowires's  $J_{sc}$  is significantly enhanced over that of the equivalent volume. In addition, figures 2(e) and (g) shows that the nanowire has a significant overall  $J$ - $V$  performance enhancement compared to the equivalent volume for a wide range of radii.

One distinctive feature in figures 2(e) and (f) is the oscillations in both the wire's  $J_{sc}$  and  $V_{oc}$  as we vary its radius. It is also important to note that the radii of the  $V_{oc}$  peaks in figure 2(e) are not co-located with the radii of the  $J_{sc}$  peaks in figure 2(f). We will elucidate these behaviors in section 5.4 below.

## 5. Physics of voltage enhancement in nanophotonic structures

In this section, we illustrate the physics of voltage enhancement in the nanophotonic structures studied in section 4. We will particularly study how the thermal emission properties of these structures influence their  $J$ - $V$  characteristics. The highlights of this section include an understanding of how absorption suppression in the immediate region above the bandgap leads to an enhancement of a thin film's voltage, how to incorporate light trapping in the thin film while maintaining its voltage enhancement, and the use of optical resonances in enhancing both the current and voltage performance of a single nanowire.

### 5.1. Bulk solar cell with anti-reflection coating

To help us illustrate the physics of voltage enhancement in nanostructures, we will first look at the thermal properties of a bulk solar cell with anti-reflection coating. We will look at the specific case of a  $10 \mu\text{m}$  thick GaAs bulk structure with multi-layer anti-reflection coating on its front surface. The absorptivity spectra of this structure is shown in figure 3. We see that its absorptivity is  $\sim 100\%$  for all incident polar angles  $\theta$  and photon energies  $E$  above the GaAs bandgap. As a result, this structure has a strong radiative generation rate and, consequently, a large  $J_{sc}$  that is close to the maximum possible  $J_{sc}$  for single-junction GaAs solar cells [58]. On the other hand, the bulk structure's strong absorptivity also gives rise to a strong thermal equilibrium radiative recombination rate  $F_{co}$  (equation (6)). Taken together, it turns out that the contrast between  $F_{sc}$

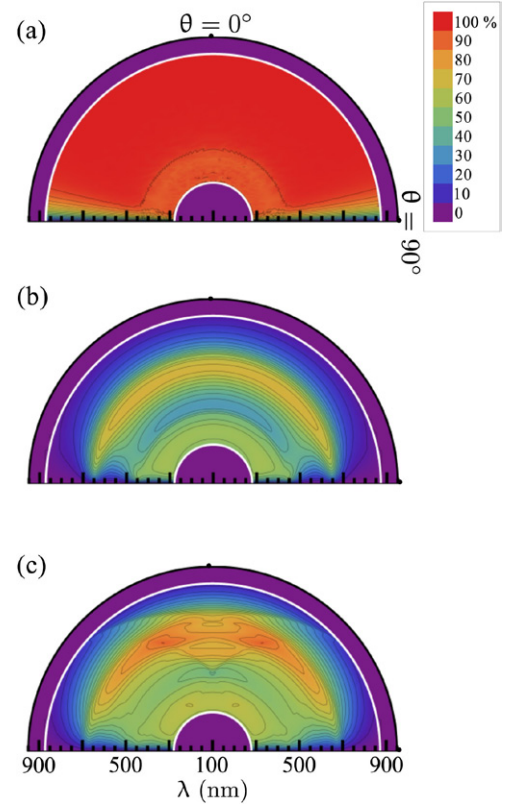


**Figure 3.** Contour-density plots of absorptivity spectra for different polar angles  $\theta$  of: (a) an  $L = 10 \mu\text{m}$  thick bulk GaAs structure with a multi-layer anti-reflection coating on its front surface, (b) thin film structure associated with the dashed  $J$ - $V$  curve in figure 1(c), and (c) grating structure associated with the solid  $J$ - $V$  curve in figure 1(c). The plot in (c) includes an integration over all azimuthal angles  $\phi$  for each polar angle  $\theta$ . The absorptivity in all plots is the mean absorptivity of the transverse electric and transverse magnetic incident polarizations. The GaAs electronic bandgap  $E_g$  is indicated by the outer white semi-circle. Reprinted with permission from [37]. Copyright 2012 The Optical Society.

and  $F_{co}$  is low, which results in a  $V_{oc}$  of 1.14 V. This  $V_{oc}$  of the bulk structure is significantly lower than the enhanced  $V_{oc}$  of the nanostructure examples presented in section 4.

### 5.2. Nanoscale flat thin-film solar cell

Figure 3(b) shows the absorptivity spectra associated with the nanoscale flat thin film introduced in section 4.1. A key difference from the bulk structure studied in section 5.1 is the strong suppression of the thin film's absorptivity in the immediate region above the bandgap. One important consequence of this absorption suppression is a large reduction of the thin film's thermal equilibrium recombination rate  $F_{co}$ . This reduction in the recombination rate can be understood by examining the spectral integration above the bandgap in (6). Particularly, since the cell is operating at the ambient temperature  $T_c$ , which satisfies  $kT_c \ll E_g$ , the thermal emission photon flux spectrum can be approximated as:

$$\Theta(E) \approx \frac{2E^2}{h^3 c^2} \exp\left(-\frac{E}{kT_c}\right) H(E - E_g) \quad (15)$$

where  $H(\cdot)$  is the Heaviside step function. Thus, the thermal emission of the cell is located immediately above the bandgap and has a relatively narrow width of  $kT_c$ . This observation suggests that reducing the cell's absorption within this narrow energy range will have a strong influence on the cell's emission rate and, therefore,  $F_{co}$ . Moreover, since the solar radiation has a much wider bandwidth, this reduction of the cell's absorption will not significantly affect the radiative generation rate  $F_s$ . Accordingly, it follows that reducing the cell's absorption in the immediate narrow energy range above the bandgap will increase the contrast between  $F_s$  and  $F_{co}$  (see (12)), leading to an enhancement of the thin film's  $V_{oc}$ .

However, figure 3(b) shows that there is also a strong reduction in the nanoscale thin film's absorption at normal incidence  $\theta = 0$  over that of the bulk structure (figure 3(a)). In addition, this absorption reduction occurs over the entire energy range above the bandgap. Consequently, the thin film's radiative generation rate  $F_s$  and, therefore, its short-circuit current in (9) is significantly reduced.

### 5.3. Nanoscale patterned thin film solar cell

The analysis in section 5.2 illustrates that the nanoscale thin film cell's  $V_{oc}$  and  $J_{sc}$  are really controlled by different parts of the absorptivity spectra. This motivates incorporating light-trapping into the thin film nanostructure with the following design criteria: (i) enhance the normal incidence absorption in order to enhance the cell's  $J_{sc}$ , while (ii) still preserving the absorption suppression in the narrow  $kT_c$  region immediately above the bandgap in order to maintain the thin film's  $V_{oc}$  enhancement over that of the bulk cell.

The optimized grating structure (introduced in section 4.2) associated with the solid  $J$ - $V$  curve in figure 1(d) and absorptivity spectra in figure 3(c) does indeed meet the above design criteria. Particularly, its absorptivity spectra does have an enhanced absorption at the normal incidence angle over that of the flat thin film, while preserving the absorption suppression for the spectral region immediately above the bandgap. This results in the grating's large  $J_{sc}$  enhancement over the thin film, while maintaining the thin film's  $V_{oc}$  enhancement over that of the bulk cell (figure 1(d)).

### 5.4. Single nanowire solar cell

We will next elucidate the single nanowire cell's voltage behavior that we presented in section 4.3. Particularly, we will show that the oscillations in the voltage and current as a function of the wire's radii in figures 2(e) and (f) are unique coherent effects arising from the wire's wave-optical properties. Furthermore, we will also show that the wire's voltage enhancement over the bulk cell is related to the removal of resonances in the immediate spectral region above the wire's material bandgap.

Normally incident light on the nanowire can couple into two linearly independent sets of leaky mode resonances that are supported by the wire [7, 63]. These are the transverse electric modes and transverse magnetic modes with the

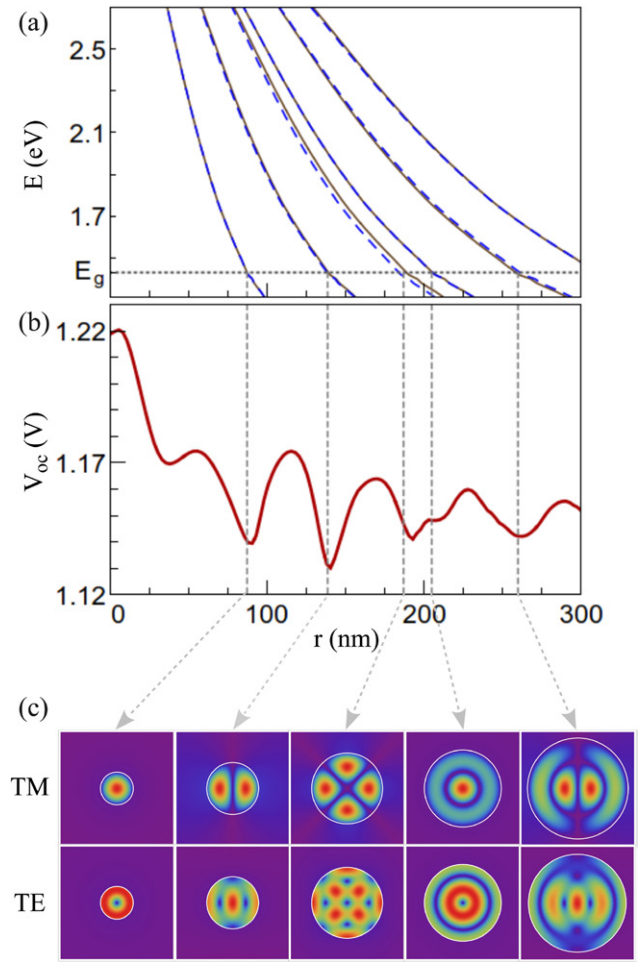


**Figure 4.** (a) Energies  $E$  of TM (solid line) and TE (dashed line) leaky mode resonances versus radius  $r$  of nanowire for normally incident ( $\theta = 0$ ) light, (b)  $V_{oc}$  versus  $r$  of nanowire, (c) TM and TE electric field across the cross-section of the nanowire around the bandgap energy  $E_g$  and at radii corresponding to the dips of the  $V_{oc}$  plot. The vertical dotted lines in (a)–(b) show that the  $V_{oc}$  dips in (b) occur when there is a leaky mode resonance in the proximity of  $E_g$ . Reprinted with permission from [34]. Copyright 2014 American Chemical Society.

magnetic field and electric field, respectively, polarized along the wire's longitudinal axis. In figure 4(a) we plot the resonant energy  $E$  of each of these supported modes as a function of the wire's radius. Generally, the resonant energies decreases with increasing radius.

In order to understand the physics that controls the  $V_{oc}$  variations in figure 2(e), figure 4 also includes a comparison between the nanowire's resonant energies  $E$  and these  $V_{oc}$  variations. We see from the plots that the location of each  $V_{oc}$  dip is at a radius where there is a resonance in the immediate vicinity of the bandgap  $E_g$ . On the other hand, the  $V_{oc}$  peaks occur at radii where there are no resonances in the immediate vicinity of  $E_g$ . Thus the  $V_{oc}$  behavior is strongly influenced by the presence or absence of resonance(s) in the immediate vicinity of  $E_g$ . This behavior is also found in the wire's absorption efficiency spectra at all angles of incidence  $\theta$  (shown in figures 5(d)–(f)), where each peak in the absorption efficiency spectra corresponds to one of the resonant



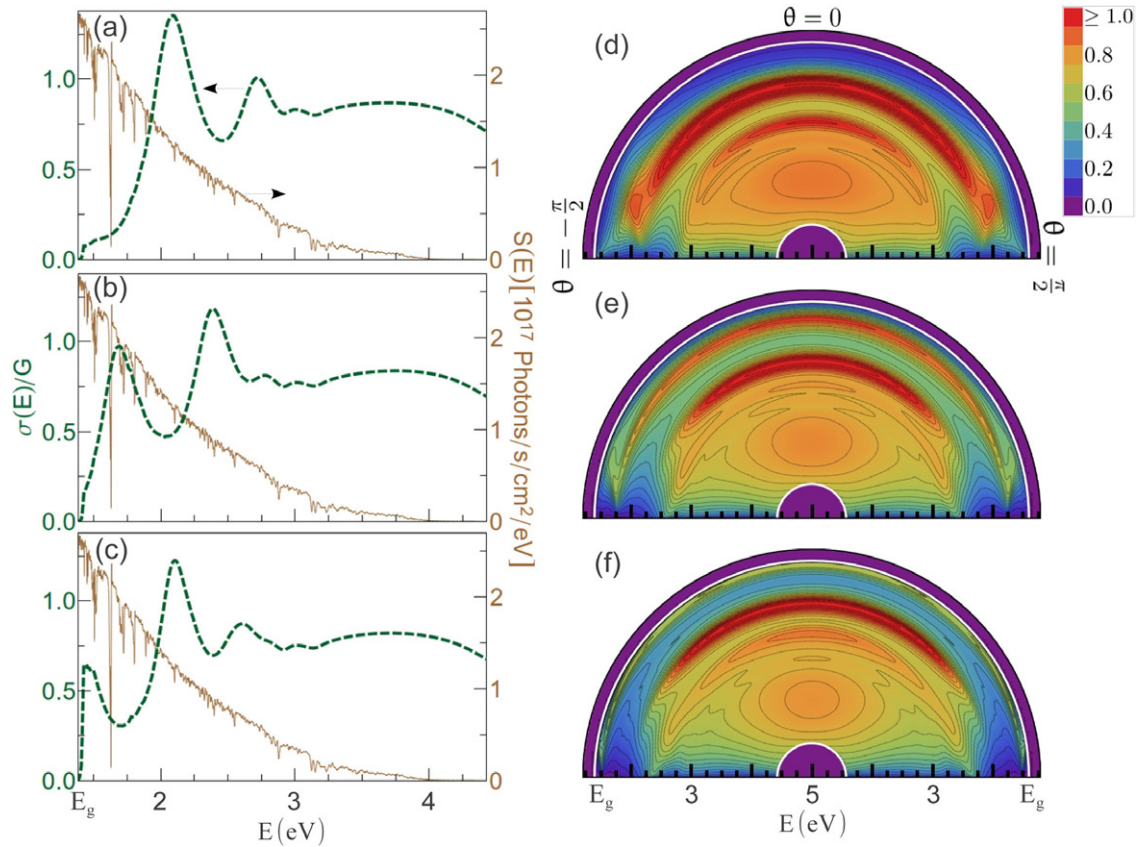


**Figure 5.** The dashed lines in (a)–(c) show the absorption efficiency  $\sigma(E)/G$  as a function of photon energy  $E$  at the normal incidence angle  $\theta = 0$  for nanowires of radii: (a)  $r = 55.5$  nm, (b)  $r = 73$  nm, and (c)  $r = 88$  nm. Each plot in (a)–(c) also includes a plot (solid line) of the Sun’s incident spectral photon flux density  $S(E)$  (equation (4)). (d)–(f) shows the  $\sigma(E)/G$  contour-density spectral plots at different incident angles  $\theta$  for nanowires with the same radii as in (a)–(c), respectively, integrated over all azimuthal angles  $\varphi$  for each angle  $\theta$ . The contours in (d)–(f) are incremented by  $\Delta\sigma(E)/G = 0.05$ . The GaAs electronic bandgap energy  $E_g$  is located at the left boundary of (a)–(c). For (d)–(f),  $E_g$  is indicated by the outer white semi-circle. Reprinted with permission from [34]. Copyright 2014 American Chemical Society.

energies in figure 4(a). For example, the spectrum for wire radius  $r = 88$  nm in figure 5(c) has its resonance located in the immediate region of the bandgap, and corresponds to a  $V_{oc}$  dip in figure 4(b). On the other hand, the other two spectra shown in figures 5(a)–(b) have their resonances located away from the bandgap, and are associated with a significantly higher  $V_{oc}$  in figure 4(b) (with radius  $r = 55$  nm having a  $V_{oc}$  oscillation peak).

This  $V_{oc}$  behavior can be explained using an argument similar to that made in section 5.2 with reference to (15). Namely, the GaAs nanowire’s thermal emittance spectral radiance has a relatively narrow width of  $kT_c$  and, therefore, its thermal equilibrium recombination rate  $F_{co}$  is strongly influenced by the absorption strength in the narrow  $kT_c$  region right above the material bandgap. Moreover, this  $kT_c$  width is a very small portion of the broadband solar spectrum and, thus, the absorption strength in this  $kT_c$  region has very little influence on the wire’s radiative generation rate  $F_s$ . Accordingly, the absence (presence) of resonances in the immediate vicinity of the bandgap increases (reduces) the wire’s  $F_s$  to  $F_{co}$  contrast and, consequently, its  $V_{oc}$ .

We next comment on the relation between the location of the resonances in figure 4(a) and the wire’s  $J_{sc}$  behavior in figure 2(f). Figures 5(a)–(c) shows the absorption efficiency

spectra for three nanowire radii around the  $J_{sc}$  oscillation peak at  $r = 73$  nm. Also included in each of figures 5(a)–(c) is the solar spectrum plot. We see that in order to have a large  $J_{sc}$ , there must be a good match between the absorption efficiency spectrum and the solar spectrum. For example, the first  $J_{sc}$  oscillation peak at  $r = 73$  nm in figure 2(f) corresponds to strong absorption resonances (figure 5(b)) located at the lower part of the usable solar spectrum where the spectral photon flux density is stronger. On the other hand, the absorption resonances in figures 5(a) and (c) are not as well matched with the solar spectrum resulting in lower  $J_{sc}$  values for those radii.

We emphasize that the oscillatory behavior of both the nanowire’s current and voltage are due to coherent effects that arise from the wire’s resonances. As the radius of the wire is increased, these oscillations become less pronounced and the wire’s  $J$ – $V$  characteristics approach that of a bulk cell.

## 6. Overcoming the Shockley–Queisser limit on efficiency in a tandem configuration by voltage enhancement

For the single-junction cells that we have studied up to now, although suppressing thermal emission in the immediate vicinity of the bandgap can lead to an increase in  $V_{oc}$ , it cannot



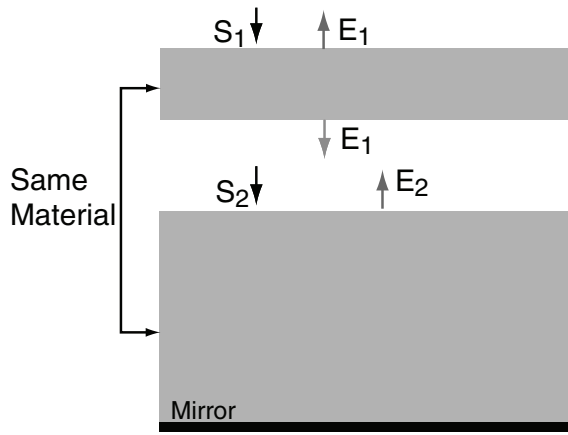


**Figure 6.** A tandem cell using a single electronic bandgap material.  $S_1$  ( $S_2$ ) is the incident sunlight absorbed by the top (bottom) cell.  $E_1$  ( $E_2$ ) is the emission of the top (bottom) cell. Reprinted with permission from [35]. Copyright 2013 American Chemical Society.

lead to any absolute maximum efficiency improvement. This is by virtue of Kirchoff's law, which requires any reduction in a cell's thermal emission to be associated with a reduction in the cell's incident light absorption (and thus a reduction of its short-circuit current). Consequently, no single-junction cell can go beyond the Shockley–Queisser limit.

On the other hand, we will outline below the recent work in [35] that shows such thermal emission engineering can indeed overcome the Shockley–Queisser limit for solar energy conversion if one adopts a tandem cell configuration, even if the multiple junctions of the tandem cell use the same material with the same electronic bandgap. We emphasize that unlike the electronic bandgap, the thermal emission of a cell is not an intrinsic property of the cell's material, but rather can be controlled via photonic design [36–38]. Therefore, the work in [35] also shows the potential of photonic design to create a single electronic bandgap tandem cell.

The structure shown in figure 6 illustrates the tandem cell configuration, which consist of a thin top cell and a thick bottom cell made from the same material, i.e. both cells have an identical electronic bandgap energy  $E_g$ . The bottom cell is assumed to absorb all incident sunlight that passes through the top cell. The bottom cell has a back mirror, and we assume perfect anti-reflection at all interfaces. To highlight the main physics, we assume that the cells have angle-independent absorption, although any such angular dependence can be straightforwardly incorporated in our analysis. We also initially neglect all non-idealities including non-radiative losses, and will comment later on the effects of including such non-idealities.

The current–voltage characteristics of the tandem cell can be derived by applying the principle of detailed balance to each cell (section 3):

$$\begin{aligned} \int_{E_g}^{\infty} dE S(E) a(E) + \int_{E_g}^{\infty} dE E_2(E, V_2) a(E) \\ = 2 \int_{E_g}^{\infty} dE E_1(E, V_1) + J_1 \end{aligned} \quad (16)$$

$$\begin{aligned} \int_{E_g}^{\infty} dE S(E) [1 - a(E)] + \int_{E_g}^{\infty} dE E_1(E, V_1) \\ = \int_{E_g}^{\infty} dE E_2(E, V_2) + J_2 \end{aligned} \quad (17)$$

where  $E_g$  is the material electronic bandgap,  $J_1$  ( $J_2$ ) is the current density of the top (bottom) cell, and  $V_1$  ( $V_2$ ) is the voltage across the top (bottom) cell. The first term in the left hand side of each equation is the respective cell's radiative generation rate due to incoming sunlight, as defined in (4). The top cell's normal incidence absorption coefficient spectrum  $a(E)$  is defined in (5).

The second term in the left hand side of each equation is the respective cell's radiative generation rate due to absorption of thermal emission originating from the opposing cell. The first term in the right hand side of each equation is the respective cell's total radiative recombination rate. The bottom cell's emission is:

$$E_2(E, V_2) = \exp\left(\frac{V_2}{kT}\right) \Theta(E, T_c) \quad (18)$$

where  $\Theta(E, T)$  is the Planck law defined in (7), and we have assumed that the bottom cell has unity absorption above photon energy  $E_g$  for all angles. The top cell's emission is:

$$E_1(E, V_1) = \exp\left(\frac{V_1}{kT}\right) \Theta(E, T_c) a(E). \quad (19)$$

where we have used Kirchoff's law to relate the top cell's emission to its absorption, and we have assumed that the top cell emits symmetrically to both its top and bottom sides in (16).

We use (16)–(17) to analyze the performance of the tandem cell shown in figure 6. The limiting efficiency is calculated by optimizing the quantity  $J_1 V_1 + J_2 V_2$ , with the assumption that both cells output power independently. For concreteness, we will specialize to GaAs material for both the top and bottom cells.

In order to establish the tandem cell's upper limit of performance, we will first consider the idealized case where the top cell has an absorption coefficient of 1 above some cutoff energy  $E_c$  that is greater than the electronic bandgap energy  $E_g$  (figure 7(a)), i.e.  $a(E) = H(E - E_c)$ . Therefore, the top cell prohibits thermal emission below the photon energy  $E_c$ . Figure 7 shows the results of solving (16)–(17) for the  $V_{oc}$  and efficiency of this idealized system for different cutoff wavelengths  $\lambda_c$  corresponding to  $E_c$ . We see that when  $\lambda_c$  is 600 nm, the tandem cell has an efficiency of 40.7%, which is much higher than the 33.2% Shockley–Queisser efficiency limit of a single-junction GaAs cell [40].

In the above idealized scenario, the limiting efficiency of our tandem cell design is equivalent to a conventional tandem cell consisting of two different materials: the top (bottom) cell having an electronic bandgap at 600 nm (880 nm). Thus, we have shown that materials of different electronic bandgaps are not necessary in order to achieve the efficiency benefits of a multi-junction cell. On the contrary, it is sufficient to just have the capability to control the thermal emission of the top cell,

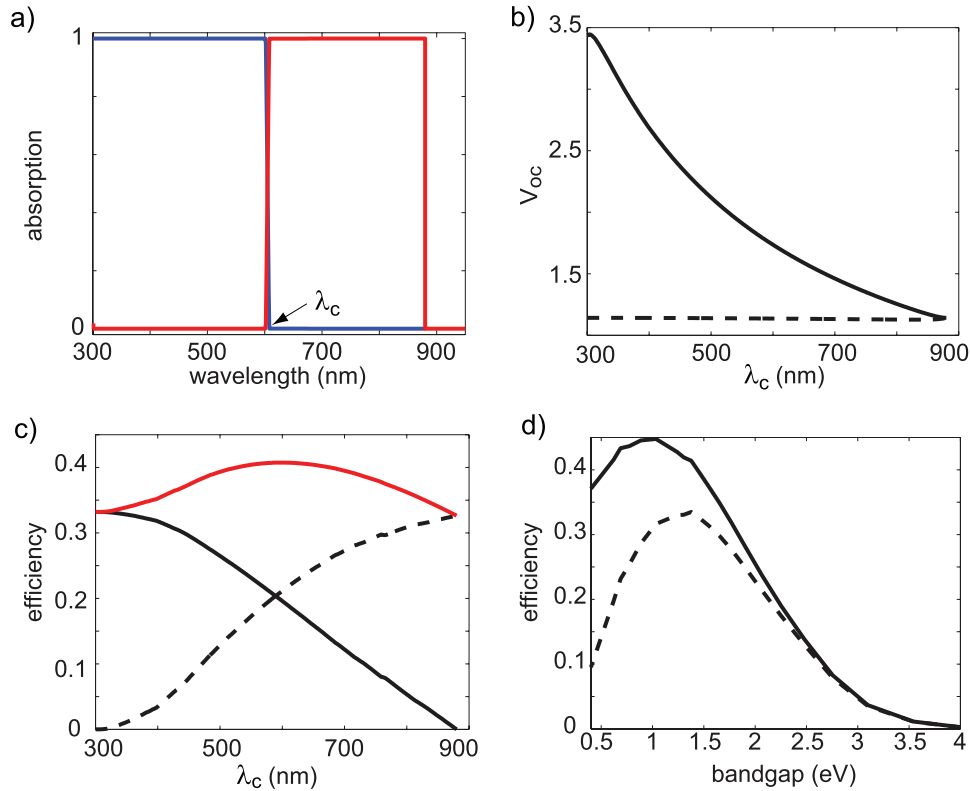


**Figure 7.** (a) The absorption spectra of the top cell (blue) and bottom cell (red) with an ideal cutoff wavelength, when the cells are placed in the tandem configuration shown in figure 6. The electronic bandgap is at 880 nm. (b) The open-circuit voltage of the top (solid) and bottom (dashed) cells as a function of cutoff wavelength  $\lambda_c$ , when both cells are operating at open-circuit. (c) The efficiency of the top cell (solid black), the bottom cell (dashed black) and the total efficiency of the tandem cell (red) as a function of  $\lambda_c$ . (d) The limiting total efficiency of a two-junction cell as a function of its electronic bandgap energy (solid line). Dashed line indicates the Shockley–Queisser limit of a single-junction cell. Reprinted with permission from [35]. Copyright 2013 American Chemical Society.

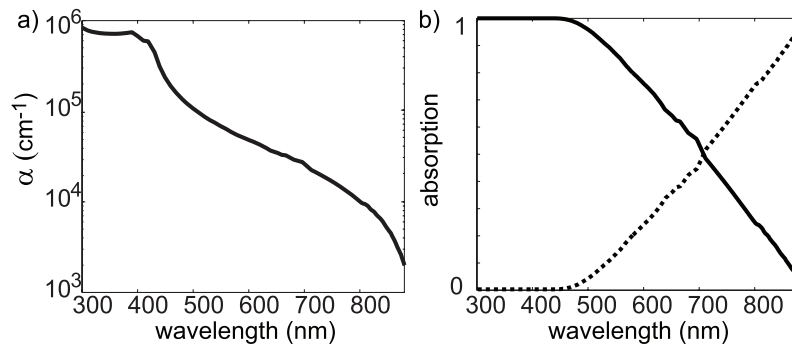


**Figure 8.** (a) Intrinsic absorption coefficient of GaAs. (b) Absorption spectra of the top cell (solid line) and the bottom cell (dashed line) when the two cells are placed in the tandem configuration shown in figure 6. The top cell consists of a GaAs film with a thickness of 300 nm. Reprinted with permission from [35]. Copyright 2013 American Chemical Society.

which can be achieved through pure photonic engineering of the top cell's geometry [36–38].

As a realistic implementation of our single bandgap GaAs tandem cell design, we will next show that we can indeed exceed the Shockley–Queisser limit in a slab geometry (figure 6). In order to simplify the analysis, we also assume that the two cells are separated by a distance larger than the optical wavelength, which ensures no near field coupling between the cells.

Figure 8(b) shows the absorption spectra of both top and bottom cells for the case where the top cell is a 300 nm thick

GaAs thin film. We see that the top cell exhibits strong absorption in the short wavelength range and a suppressed emission near  $E_g$ , thus satisfying the requirements above for achieving a tandem cell with efficiency beyond the Shockley–Queisser limit.

Figure 9 illustrates the impact of the top cell's thickness on the tandem cell's  $J$ – $V$  performance. We see in figure 9(a) that the tandem cell's total efficiency peaks at 33.74% when the top cell has a thickness of 300 nm, assuming a four-terminal connection where each cell outputs independently. This peak efficiency is significantly higher than the 33.2%

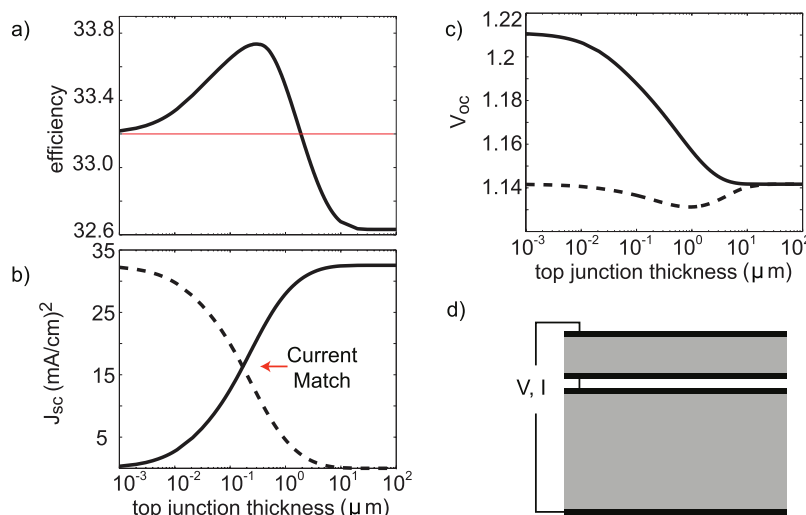


**Figure 9.** (a) Plots show total efficiency of the tandem cell as a function of top cell's thickness (black line), and Shockley–Queisser limit for the efficiency of a single-junction GaAs cell (red line). (b) Short-circuit current of the top (solid line) and bottom (dashed line) cells. (c) Open-circuit voltage of the top (solid line) and bottom (dashed line) cells. (d) Tandem cell with serial connection. Reprinted with permission from [35]. Copyright 2013 American Chemical Society.

Shockley–Queisser limit for a GaAs single-junction cell under direct sunlight. Moreover, it is also higher than the 33.5% Shockley–Queisser limit of any single-junction cell under direct sunlight [40, 58]. Therefore we see that even a relatively simple two-junction GaAs tandem cell geometry can achieve efficiencies beyond the Shockley–Queisser limit. Furthermore, at the peak efficiency, the top cell has an open-circuit voltage of 1.174 V, which is significantly higher than the open-circuit voltage of a single-junction bulk GaAs cell [38].

In the case of a serial connection (figure 9(d)), a 160 nm thick top cell can give current matching with a  $16.63 \text{ mA cm}^{-2}$  current output for each cell. The  $V_{oc}$  and efficiency of this serially connected cell are 2.317 V and 33.71%, respectively. Therefore, a two-terminal serially connected tandem cell can achieve the same theoretical efficiency as the four-terminal case.

The behavior of the tandem cell's efficiency can be understood by analyzing the effect of the top cell's thickness on the  $J$ – $V$  performance of each cell component of the tandem cell. Generally, the  $J_{sc}$  of the top (bottom) cell increases (decreases) with an increase in the top cell's thickness, due to an increase in the top cell's absorption of incident sunlight (figure 9(b)). Furthermore, the top cell's  $V_{oc}$  increases with a decrease in the top cell's thickness, due to a decrease in the top cell's thermal emission in the immediate vicinity of the bandgap. On the other hand, a change in the top cell's thickness does not strongly influence the bottom cell's thermal emission and therefore its  $V_{oc}$ .

However, when the top cell's thickness is reduced below 300 nm, its  $J_{sc}$  reduces (figure 9(b)) in spite of its  $V_{oc}$  enhancement (figure 9(c)), since there is a significant reduction of the top cell's absorption of incident sunlight. Consequently in this top cell's small thickness regime, the tandem cell's total efficiency is mainly determined by the bottom cell's  $J$ – $V$  performance alone. This total efficiency approaches the 33.2%

Shockley–Queisser limit of a GaAs single-junction solar cell as the top cell's thickness approaches zero (figure 9(a)). On the other hand, when the top cell's thickness exceeds  $10 \mu\text{m}$ , the tandem cell's efficiency is determined mainly by the top cell, since the top cell absorbs almost all the incoming sunlight. In this top cell's large thickness regime, the tandem cell's total efficiency of 32.63% is slightly lower than the single-junction Shockley–Queisser limit, because of the additional emission from the top cell's bottom side [58]. Nevertheless, we emphasize that the tandem cell's total efficiency is above the Shockley–Queisser limit (red line in figure 9(a)) as long as the top cell's thickness is below  $1.9 \mu\text{m}$ .

The supplementary document to [35] includes a detailed discussion on adding non-radiative recombination into the above analysis of the tandem cell. Generally, the leading intrinsic non-radiative loss in GaAs is Auger recombination. However, even for a 300 nm thick top cell, the inclusion of this Auger recombination results in a negligible degradation of the cell's voltage and, therefore, its efficiency (section 3.1).

## References

- [1] Green M A 2003 *Third Generation Photovoltaics: Advanced Solar Energy Conversion* (New York: Springer)
- [2] Li J, Wang D and LaPierre R R 2011 *Advances in III–V Semiconductor Nanowires and Nanodevices* (Oak Park, IL: Bentham Science)
- [3] Yan R, Gargas D and Yang P 2009 *Nat. Photonics* **3** 569–76
- [4] Garnett E C, Brongersma M L, Cui Y and McGehee M D 2011 *Annu. Rev. Mater. Res.* **41** 269–95
- [5] Kempa T J, Cahoon J F, Kim S K, Day R W, Bell D C, Park H G and Lieber C M 2012 *Proc. Natl Acad. Sci. USA* **109** 1407–12
- [6] Krogstrup P, Jorgensen H I, Heiss M, Demichel O, Holm J V, Aagesen M, Nygard J and Fontcuberta I Morral A 2013 *Nat. Photonics* **7** 1749–4885
- [7] Cao L, White J S, Park J S, Schuller J A, Clemens B M and Brongersma M L 2009 *Nat. Mater.* **8** 643–7

- [8] Hochbaum A I and Yang P 2010 *Chem. Rev.* **110** 527–46 (pMID: 19817361)
- [9] Zhu J, Hsu C M, Yu Z, Fan S and Cui Y 2010 *Nano Lett.* **10** 1979–84 (pMID: 19891462)
- [10] Atwater H A 2011 Paths to high efficiency low-cost photovoltaics 37th *IEEE Photovoltaic Specialists Conf. (PVSC)* 000001–3
- [11] Shah A, Torres P, Tschanner R, Wyrsh N and Keppner H 1999 *Science* **285** 692–8
- [12] Pillai S, Catchpole K R, Trupke T and Green M A 2007 *J. Appl. Phys.* **101** 093105
- [13] Hu L and Chen G 2007 *Nano Lett.* **7** 3249–52
- [14] Chutinan A and John S 2008 *Phys. Rev. A* **78** 023825
- [15] Zeng L, Bermel P, Yi Y, Alamariu B A, Broderick K A, Liu J, Hong C, Duan X, Joannopoulos J and Kimerling L C 2008 *Appl. Phys. Lett.* **93** 221105
- [16] Lin C and Povinelli M L 2009 *Opt. Express* **17** 19371–81
- [17] Saeta P N, Ferry V E, Pacifici D, Munday J N and Atwater H A 2009 *Opt. Express* **17** 20975–90
- [18] Pala R A, White J, Barnard E, Liu J and Brongersma M L 2009 *Adv. Mater.* **21** 3504–9
- [19] Mallick S B, Agrawal M and Peumans P 2010 *Opt. Express* **18** 5691–706
- [20] Sheng X, Johnson S G, Michel J and Kimerling L C 2011 *Opt. Express* **19** A841–50
- [21] Raman A, Yu Z and Fan S 2011 *Opt. Express* **19** 19015–26
- [22] Martins E R, Li J, Liu Y, Zhou J and Krauss T F 2012 *Phys. Rev. B* **86** 041404
- [23] McPheeters C O and Yu E T 2012 *Opt. Express* **20** A864–78
- [24] Green M A 1993 *Semicond. Sci. Technol.* **8** 1
- [25] Narayanan S and Green M 1989 *Sol. Cells* **26** 329–34
- [26] Lei P H, Lin C T and Ye S J 2013 *J. Phys. D: Appl. Phys.* **46** 125105
- [27] Bailey C G, Forbes D V, Polly S J, Bittner Z S, Dai Y, Mackos C, Raffaele R P and Hubbard S M 2012 *IEEE J. Photovolt.* **2** 269–75
- [28] Yang P, Zeng X, Xie X, Zhang X, Li H and Wang Z 2013 *RSC Adv.* **3** 24971–4
- [29] Luque A, Marti A and Stanley C 2012 *Nat. Photonics* **6** 146–52
- [30] Ray B, Lundstrom M S and Alam M A 2012 *Appl. Phys. Lett.* **100** 013307
- [31] Sun Y, Yang J, Yang L, Cao J, Gao M, Zhang Z, Wang Z and Song H 2013 *J. Solid State Chem.* **200** 258–64
- [32] Hsiao K J 2014 *Sol. Energy Mater. Sol. Cells B* **120** 647–53
- [33] Anttu N 2015 *ACS Photonics* **2** 446–53
- [34] Sandhu S, Yu Z and Fan S 2014 *Nano Lett.* **14** 1011–5
- [35] Yu Z, Sandhu S and Fan S 2014 *Nano Lett.* **14** 66–70 (PMID: 24279726)
- [36] Munday J N 2012 *J. Appl. Phys.* **112** 064501
- [37] Sandhu S, Yu Z and Fan S 2013 *Opt. Express* **21** 1209–17
- [38] Niv A, Gharghi M, Gladden C, Miller O D and Zhang X 2012 *Phys. Rev. Lett.* **109** 138701
- [39] Yu Z, Raman A and Fan S 2010 *Proc. Natl Acad. Sci. USA* **107** 17491–6
- [40] Shockley W and Queisser H J 1961 *J. Appl. Phys.* **32** 510–9
- [41] Markvart T 2008 *J. Opt. A: Pure Appl. Opt.* **10** 015008
- [42] Kosten E D, Atwater J H, Parsons J, Polman A and Atwater H A 2013 *Light Sci. Appl.* **2** e45
- [43] Rytov S M, Kravtsov Y A and Tatarskii V I 1989 *Principles of Statistical Radiophysics* **3** 1st ed (New York: Springer)
- [44] Luo A, Narayanaswamy A, Chen G and Joannopoulos J D 2004 *Phys. Rev. Lett.* **93** 213905
- [45] (NREL) N R E L 2008 Air mass 1.5 (am1.5) global spectrum (astm173-03g) <http://rredc.nrel.gov/solar/spectra/am1.5/>
- [46] Bohren C F and Huffman D R 1983 *Absorption and Scattering of Light by Small Particles* 1st ed (New York: Wiley)
- [47] Landau L D and Lifshitz E M 1980 *Statistical Physics Part 1* 3rd edn (Burlington, MA: Elsevier)
- [48] Landau L D and Lifshitz E M 1993 *Electrodynamics of Continuous Media* 2nd edn (Burlington, MA: Elsevier)
- [49] Liu V and Fan S 2012 *Comput. Phys. Commun.* **183** 2233–44
- [50] Shin W and Fan S 2012 *J. Comput. Phys.* **231** 3406–31
- [51] Shockley W and Read W T 1952 *Phys. Rev.* **87** 835–42
- [52] Hall R N 1952 *Phys. Rev.* **87** 387
- [53] Sze S M and Lee M K 2012 *Semiconductor Devices: Physics and Technology* 3rd edn (New York: Wiley) p 62 (chapter 2)
- [54] Chang C C *et al* 2012 *Nano Lett.* **12** 4484–9
- [55] Tajik N, Peng Z, Kuyanov P and LaPierre R R 2011 *Nanotechnology* **22** 225402
- [56] Mariani G, Scofield A and Huffaker D 2012 High-performance patterned arrays of core-shell gaas nanopillar solar cells with in situ ingap passivation layer 38th *IEEE Photovoltaic Specialists Conf.* pp 003080–2
- [57] Huang N, Lin C and Povinelli M L 2012 *J. Appl. Phys.* **112** 064321
- [58] Miller O D, Yablonovitch E and Kurtz S R 2012 *IEEE J. Photovolt.* **2** 303–11
- [59] Green M 1984 *IEEE Trans. Electron Devices* **31** 671–8
- [60] Tiedje T, Yablonovitch E, Cody G D and Brooks B G 1984 *IEEE Trans. Electron Devices* **31** 711–6
- [61] Kayes B, Nie H, Twist R, Spruytte S, Reinhardt F, Kizilyalli I and Higashi G 2011 27.6% conversion efficiency, a new record for single-junction solar cells under 1 sun illumination 37th *IEEE Photovoltaic Specialists Conf. (PVSC)* 000004–8
- [62] Palik E D 1985 *Handbook of Optical Constants of Solids* vol **1** (Waltham, MA: Elsevier Academic Press) p 436
- [63] Snyder A W and Love J D 1983 *Optical Waveguide Theory* 1st edn (London: Chapman and Hall)